The Astrophysical Journal, 856:74 (11pp), 2018 March 20 https://doi.org/10.3847/1538-4357/aab3e0

Demonstration of a Novel Method for Measuring Mass-loss Rates for Massive Stars

Henry A. Kobulnicky[1], William T. Chick[1], and Matthew S. Povich[2]
[1] Department of Physics & Astronomy, University of Wyoming, Dept 3905, Laramie, WY 82070-1000, USA; chipk@uwyo.edu
[2] Department of Physics & Astronomy, California State Polytechnic University, 3801 West Temple Avenue, Pomona, CA 91768, USA
Received 2018 February 7; revised 2018 March 1; accepted 2018 March 1; published 2018 March 27

Abstract

The rate at which massive stars eject mass in stellar winds significantly influences their evolutionary path. Cosmic rates of nucleosynthesis, explosive stellar phenomena, and compact object genesis depend on this poorly known facet of stellar evolution. We employ an unexploited observational technique for measuring the mass-loss rates of O and early-B stars. Our approach, which has no adjustable parameters, uses the principle of pressure equilibrium between the stellar wind and the ambient interstellar medium for a high-velocity star generating an infrared bow shock nebula. Results for 20 bow-shock-generating stars show good agreement with two sets of theoretical predictions for O5–O9.5 main-sequence stars, yielding $\dot{M} = 1.3 \times 10^{-6}$ to 2×10^{-9} $M_{\odot}$ yr^{-1}. Although $\dot{M}$ values derived for this sample are smaller than theoretical expectations by a factor of about two, this discrepancy is greatly reduced compared to canonical mass-loss methods. Bow-shock-derived mass-loss rates are factors of 10 smaller than Hα-based measurements (uncorrected for clumping) for similar stellar types and are nearly an order of magnitude larger than P^{4+} and some other diagnostics based on UV absorption lines. Ambient interstellar densities of at least several cm^{-3} appear to be required for formation of a prominent infrared bow shock nebula. Measurements of $\dot{M}$ for early-B stars are not yet compelling owing to the small number in our sample and the lack of clear theoretical predictions in the regime of lower stellar luminosities. These results may constitute a partial resolution of the extant "weak-wind problem" for late-O stars. The technique shows promise for determining mass-loss rates in the weak-wind regime.

Key words: catalogs – H II regions – stars: massive – surveys

1. Introduction

Massive stars shed mass prodigiously via their radiation-driven stellar winds (Lucy & Solomon 1970; Castor et al. 1975; Pauldrach et al. 1986) and perhaps even more dramatically through pulsationally driven ejection events (Glatzel et al. 1999; Kraus et al. 2015; Yadav & Glatzel 2017). For single massive stars, the mass-loss rate, $\dot{M}$, integrated over the star's lifetime determines its final act (i.e., type of supernova or γ-ray burst), end product (i.e., neutron star, black hole, none), and its radiant and nucleosynthetic contribution to the cosmos. For the $\simeq$50% of massive stars having a close companion (Sana et al. 2012; Kobulnicky et al. 2014), the effects of mass exchange and common envelope evolution are expected to be a more significant evolutionary influence, but wind-driven mass loss must still play a large role when integrated over the lifetime of a star. Observational and theoretical work broadly agree that mass-loss rates range from $<10^{-8}$ $M_{\odot}$ yr^{-1} for weak-winded late-O stars to a few $\times 10^{-5}$ $M_{\odot}$ yr^{-1} for the most luminous, evolved massive stars, with rates being factors of several lower at low metallicities (Vink et al. 2001; Martins et al. 2005b; Fullerton et al. 2006; Mokiem et al. 2007; Muijres et al. 2012; Massa et al. 2017). Luminous blue variables and related objects in unstable phases of evolution may eject shells from several tenths to several solar masses in discrete eruptive events, resulting in time-averaged rates of 0.01 to a few $M_{\odot}$ yr^{-1} (Smith & Owocki 2006). Such large excretion events influence not only the evolution of the star but the appearance of subsequent explosive phenomena, such as when fast supernova ejecta encounter dense circumstellar material, creating unusually luminous supernovae (Smith & McCray 2007; Miller et al. 2009; Chevalier & Irwin 2011). Given that most massive stars are also members of (close!) multiple systems (Kobulnicky & Fryer 2007; Sana et al. 2012; Kobulnicky et al. 2016), companion interactions are certain to play an important (but poorly characterized, at present) role. Reviews of massive star winds and mass loss include Kudritzki & Puls (2000), Puls et al. (2008), and Smith (2014).

Mass-loss rates for massive stars have been measured using a variety of techniques. These include observations of Hα recombination lines (Leitherer 1988; Lamers & Leitherer 1993; Puls et al. 1996; Markova et al. 2004; Martins et al. 2005b) and radio-continuum and infrared free–free emission (Abbott et al. 1981; Nugis et al. 1998; Puls et al. 2006; Massa et al. 2017), which are so-called n^2 diagnostics because the excess flux scales as the square of the density of material in the wind. Massive star winds are demonstrably not ideal isotropic structures with smooth density gradients. Observational signatures of density inhomogeneities (i.e., "clumping") in OB-star winds are abundant, including time-variable line profiles and discrete absorption components (Ebbets 1982; Fullerton et al. 1996; Lépine & Moffat 1999; Prinja et al. 2002), especially in supergiants, and the presence of large-scale, optically thick clumps (Prinja & Massa 2010). Accordingly, the presence of clumps, which result inevitably from instabilities in the line-driven wind (Owocki et al. 1988; Dessart & Owocki 2005; Muijres et al. 2011), may skew observationally determined mass-loss estimates upward relative to unclumped calculations. Although theoretical models for stellar winds include provisions for clumping in a heuristic way (e.g., Hillier & Miller 1998; Puls et al. 2005), the poorly constrained clump geometries and kinematics introduce uncertainties of one or two orders of magnitude in the mass-loss rates from n^2 diagnostics. Furthermore, the traditional n^2 diagnostics become insensitive to mass loss below rates of about 10^{-7} $M_{\odot}$ yr^{-1} (Markova et al. 2004; Mokiem et al. 2007;

Marcolino et al. 2009), corresponding to luminosities of about $10^{5.2}$ (approximately an O7.5V), demanding other diagnostics for the weaker winds expected from less luminous stars.

Ultraviolet spectroscopy of metal resonance lines such as C III, N V, Si IV, and P V has provided the other major diagnostic of mass-loss rates (Garmany et al. 1981; Howarth & Prinja 1989; Fullerton et al. 2006; Marcolino et al. 2009). UV-based estimates of mass loss are less sensitive to clumping because they depend linearly on density as long as the optical depths in the line cores are small and the dominant ionization species can be observed. Mass-loss rates derived from UV resonance lines are often factors of several to hundreds lower than n^2 diagnostics (Fullerton et al. 2006) in the limited regimes where the two methods overlap. For mass-loss rates greater than about 10^{-7} $M_\odot$ yr^{-1}, resonance lines begin to become optically thick and derived $\dot{M}$ values become less certain, especially if clumping is optically thick (Prinja & Massa 2010). UV estimates may also be systematically low if coronal X-rays produce additional photoionization of the metal ionic species probed by UV spectra and ionization correction factors are not properly applied (Waldron 1984; Marcolino et al. 2009; Huenemoerder et al. 2012).

Theoretical mass-loss rates predicted on the basis of the "modified wind momentum"[3] (Puls et al. 1996; Vink et al. 2001) agree with observations in the limit of strong winds and luminous stars (i.e., $\log(L/L_\odot) \gtrsim 5.2$, spectral type earlier than about O7V), but in the limit of weak winds ($\dot{M} \lesssim 10^{-8}\,M_\odot$ yr^{-1}, $\log(L/L_\odot) \lesssim 5.2$), UV-derived mass-loss rates are lower than theoretical predictions by up to two orders of magnitude—a discrepancy known as the "weak-wind problem," discussed extensively in the literature (Martins et al. 2005b; Mokiem et al. 2007; Marcolino et al. 2009; Muijres et al. 2012). Whether the discrepancy results from the effects of clumping, unexpected ionization structure, variations in $\dot{M}$ as a star evolves, limitations in the theoretical treatment of the wind (Lucy 2010a; Krtička & Kubát 2017), or some combination, remains a matter of debate. In the limit of very massive and luminous supergiants near 50 $M_\odot$, the Vink & Gräfener (2012) "transition mass-loss rate" near 10^{-5} $M_\odot$ yr^{-1} suggests that the current reductions of two to three in model mass-loss rates is appropriate. However, much of the O-star regime remains uncertain. The recognition that some late-O stars exhibit much weaker winds than other O stars of the same spectral type is regarded as a kind of second-order weak-wind problem (Marcolino et al. 2009) that might be solved along with the resolution of the canonical weak-wind problem. Huenemoerder et al. (2012) presented one possible resolution in their study of the weak-wind O9.5V runaway star μ Col, which evinces a massive, hot stellar wind visible in X-rays but only tenuously detectable using UV metal absorption-line spectroscopy.

Given the lingering order-of-magnitude uncertainties on mass-loss rates, together with the sensitivity[4] of stellar and cosmic evolution to these values, alternative observational diagnostics for $\dot{M}$ are warranted. Kobulnicky et al. (2010) proposed using runaway (Blaauw 1961; Gies & Bolton 1986) massive stars and their interstellar bow shock nebulae (van Buren & McCray 1988; Noriega-Crespo et al. 1997; Gvaramadze & Bomans 2008) as a new laboratory for measuring mass-loss rates. Following the reasoning first articulated by Gull & Sofia (1979) for the prototypical bow shock runaway star ζ Oph, we employ the principle of balancing the momentum flux between the stellar wind and the impinging interstellar material:

$$\rho_w V_w^2 = \rho_a V_a^2. \quad (1)$$

Here, ρ_w is the density of the stellar wind, V_w is the velocity of the wind, ρ_a is the ambient interstellar density, and V_a is the velocity of the ambient interstellar medium (ISM) in the rest frame of the star. We make the assumption that the stellar wind is isotropic (but mass loss could be enhanced along the polar axis or reduced at the equatorial plane for rapidly rotating stars; Owocki et al. 1996; Langer 1998; Müller & Vink 2014) so that the density of the stellar wind can be expressed as

$$\rho_w = \frac{\dot{M}}{4\pi R_0^2 V_w}\ , \quad (2)$$

where $\dot{M}$ is the stellar mass-loss rate and R_0 is the "standoff" radius—the distance between the star and the point where the momentum fluxes are equal. By substitution of Equation (2) into Equation (1) and rearranging, the mass-loss rate can be expressed in terms of observable stellar and interstellar properties:

$$\dot{M} = \frac{4\pi R_0^2 V_a^2 \rho_a}{V_w}. \quad (3)$$

Here, R_0 is simply R_{0r} D, the angular size of the standoff distance in radians times the distance to the star. The former is straightforward to measure from infrared images, modulo the unknown factor for inclination; arguably $\sin i \simeq 1$ so that the bow shocks can be identified as arcuate nebulae (Kobulnicky et al. 2017). Distances, D, may be obtained by spectroscopic parallax or by geometric parallax measurements (Perryman et al. 1997; Gaia Collaboration et al. 2016a, 2016b). The term V_w is taken to be the terminal stellar wind speed, V_∞, appropriate to the spectral type and luminosity class, as tabulated in the literature (e.g., Mokiem et al. 2007), although individual stars may vary significantly about the mean. Note that V_a is expected to average 30 km s^{-1} for runaway stars, but individual values may again vary significantly. "In situ" bow shocks (Povich et al. 2008; Sexton et al. 2015), where the relative motion is caused by an outflow of interstellar material at 10–15 km s^{-1} from a H II region (e.g., the Carina star-forming region; Walborn et al. 2002) rather than a runaway star, could be such exceptions. Specific space velocities for any star may ordinarily be calculated from measurements of proper motions, radial velocities, and distances. The ambient ISM density is the most challenging quantity to measure. Gvaramadze et al. (2012) applied this technique, using the size of the H II region surrounding ζ Oph and its ionizing flux to eliminate the ambient density in Equation (3) (or equivalently, solve for it numerically). They derived a mass-loss rate of $2.2 \times 10^{-8}\,M_\odot$ yr^{-1}, comparable to updated theoretical predictions of Lucy (2010a). However, they note that H II regions are not generally present around bow-shock-producing stars, limiting the utility of this approach to

[3] The modified wind momentum is $\dot{M} v_\infty (R_*/R_\odot)^{0.5}$, where v_∞ is the terminal stellar wind velocity, and R_* is the stellar radius, after Puls et al. (1996).

[4] Changing mass-loss rates by factors of two or less can dramatically alter the sequence of stellar evolutionary phases, final masses, stellar endpoints, and nucleosynthetic yields (e.g., Meynet et al. 1994, 2015; Renzo et al. 2017)!

measuring ρ_a. Here, we use the peak infrared surface brightness of the nebula to estimate ρ_a, as described in subsequent sections.

In this contribution, we apply the principle of momentum balance to derive mass-loss rates for the 20 bow-shock-producing stars having well-characterized stellar parameters from Table 5 of Kobulnicky et al. (2017). As an independent technique for estimating mass loss, our method does not depend on requirements like optically thin atomic lines, the adopted geometrical parameterization of clumping, or a detailed treatment of the ionization structure in the wind. Massive stars are known to exhibit temporal variability in their line profiles, indicating probable variation in clumping and mass loss. We expect that our approach has the added benefit of averaging over short-term fluctuations in wind structure and mass-loss rate. This method will undoubtedly entail a different suite of uncertainties and potential biases than the traditional ones, including the difficult-to-parameterize effects of a star moving through a nonuniform ambient ISM, a possibility that we neglect in this initial treatment. Nevertheless, most of our targets are late-O dwarf stars, making this sample especially relevant for addressing the weak-wind problem. In Section 2 we describe our methods for determining the requisite stellar and interstellar parameters. In Section 3 we present new mass-loss rates for this well-characterized sample of stars and compare them to existing observational and theoretical determinations for stars of similar luminosity and evolutionary stage. Section 4 summarizes implications for these new results and outlines prospects for future progress.

2. Measuring $\dot{M}$

2.1. Sample Selection

Table 1 lists the 20 stars from Table 5 of Kobulnicky et al. (2017) selected from among the 709 bow shock candidates of Kobulnicky et al. (2016) as having secure distances, spectral types, and infrared photometric measurements[5] at multiple bandpasses covering the adjoining nebula. Column 1 contains the index number using the numeration of Kobulnicky et al. (2016). Column 2 lists the common name of the star, followed by the generic name in galactic coordinates in column 3. Columns 4 and 5 provide the adopted spectral type/luminosity class and corresponding literature references, respectively. Only three or four objects have evidence for being part of a multiple-star system. This is significant because it means that, in the majority of systems, one star is the dominant source of stellar wind, thereby simplifying any ensuing interpretation. Columns 6 and 7 contain the adopted effective temperatures and radii, using the theoretical O-star temperature scale (Tables 1–3) of Martins et al. (2005a). For the few B stars, we use the temperatures and radii of Pecaut & Mamajek (2013). Column 8 gives the adopted stellar mass. Column 9 provides the adopted terminal wind speed calculated by averaging galactic O and B stars of the same spectral type from Table A.1 of Mokiem et al. (2007) and Table 3 of Marcolino et al. (2009). These values are uncertain at the level of 50%, based on the dispersion among multiple measurements at a given spectral type. Early-B dwarfs are particularly uncertain owing to the difficulty in measuring wind lines. Column 10 lists the adopted distance along with the corresponding reference in column 11. Most the sources have distances estimated through their association with a star cluster or molecular cloud having distance measurements from eclipsing binaries (such as in Cygnus OB2), main-sequence fitting, or radio very long baseline interferometry (VLBI) geometric parallaxes of masers within the adjoining star-forming complex. The O8V KGK2010 10 deserves special mention. At $\ell = 77\overset{\circ}{.}0$, $b = -0\overset{\circ}{.}6$, it lies more than two degrees from the main body of the Cygnus OB2 Association—outside the nominal boundaries of the Cygnus-X star-forming complex and possibly at a different distance. At $V = 15$ mag it is also 2–3 mag fainter at the V band than other O8V stars of similar reddening (see Massey & Thompson 1991, Table 5) in Cygnus OB2. It may be a background object at a distance similar to Cygnus X-3 (Ling et al. 2009, 3.4 kpc or 9.3 kpc). Based on its reddening ($A_V = 5.4$ mag) similar to other $V \approx 12.5$ O8V stars in Cygnus OB2 at 1.32 kpc (Kiminki et al. 2015), we use the factor of 9.8 in flux, corresponding to a factor of 3.1 in distance, to adopt a scaled distance of 4.1 kpc, while cautioning of a more uncertain distance for this object. Column 12 lists the standoff distance, R_0, in arcsec, while column 13 lists the standoff distance in pc, calculated from the distance in column 10 and the angular separation.[6] Column 14 lists the peak *HSO* 70 μm surface brightness above adjacent background levels in Jy sr^{-1}, occurring at a location near the apex of the nebula. We use the 70 μm measurement because the majority of bow shock candidates are detected and stochastic heating effects are unlikely to affect dust at this wavelength compared to 24 μm. Column 15 lists angular diameter in arcsec of the nebulae along a chord (l) intersecting the peak surface brightness. Figure 1 shows the G078.2889+00.7829 nebula surrounding the central star LS II+39 53 (O7V). Red, green, and blue depict the *HSO* 160 and 70 μm and *SST* 24 μm data, respectively. The white asterisk marks the location of the central star. White lines represent the standoff distance, R_0, and the chord diameter, ℓ.

2.2. Calculation of $\dot{M}$

Beginning with Equation (3), we express the standoff distance, R_0, as the product of the distance to the source, D, times the angular distance from star to apex in radians, R_{0r}. Given that very few bow shock stars have measured space velocities, we adopt for V_a a typical "runaway" speed of 30 km s^{-1} (Gies & Bolton 1986). For ζ Oph we adopt the 26.5 km s^{-1} calculated from its proper motion and radial velocity (Gvaramadze et al. 2012). Velocities much smaller than this are unlikely to produce bow shocks, while stars moving much faster than this would fall on the tail of the Maxwell–Boltzmann velocity distribution and be quite rare. Thirty kilometers per second agrees well with the measured space velocity for the nearest bow shock star, ζ Oph (Gvaramadze et al. 2012), and is a reasonable average value in the absence of individual data. The ambient interstellar density, ρ_a, can be expressed as $n_a\bar{m}$, the ambient number density and mean particle mass, respectively. We adopt $\bar{m} = 2.3 \times 10^{-24}$ g, appropriate to the Milky Way ISM. While the ambient number density n_a preceding the bow shock is challenging to measure, the density within a bow shock nebula, n_N, can be estimated

[5] Photometric data include a measurement at the *Wide-Field Infrared Explorer (WISE)* 22 μm band or *Spitzer Space Telescope (SST)* 24 μm band and the *Herschel Space Observatory (HSO)* 70 μm band.

[6] We apply a statistical correction factor of $1/\sin(65°) = 1.10$ for geometrical projection effects when computing R_0 in pc. This is a suitable correction because inclinations substantially smaller than about 50° would begin to mask the bow shock morphology and make the object unlikely to be included in the list of bow shock candidates (e.g., see Acreman et al. 2016 for numerical simulations of bow shocks at various inclination angles).

Table 1
Measured and Adopted Parameters for Stars and Their Bow Shock Nebulae

ID	Name	Alt. name	Sp.T.	Ref.	$T_{\rm eff}$ (K)	R_* ($R_\odot$)	Mass ($M_\odot$)	V_∞ (km s^{-1})	D (kpc)	Ref.	R_0 (arcsec)	R_0 (pc)	Peak$_{70}$ (10^7 Jy sr^{-1})	ℓ (arcsec)
(1)	(2)	(3)	(4)	(5)	(6)	(7)	(8)	(9)	(10)	(11)	(12)	(13)	(14)	(15)
13	ζ Oph	G006.2812+23.5877	O9.2IV	S1	31000	10	19	1300	0.11	D1	299	0.175	12.3	277
67	NGC 6611 ESL 45	G017.0826+00.9744	O9V	S2	31500	7.7	18	1300	1.99	D2	7.5	0.080	64.0	15
329	KGK2010 10	G077.0505−00.6094	O8V	S3	33400	8.5	23	2000	4.1	D3[a]	10	0.219	15.4	27
331	LS II +39 53	G078.2869+00.7780	O7V	S4	35500	9.3	26	2500	1.32	D3[a]	42	0.296	12.0	55
338	CPR2002A10	G078.8223+00.0959	O8V:	S3	33400	8.5	23	1200	1.32	D3[a]	23	0.162	79.8	29
339	CPR2002A37	G080.2400+00.1354	O5V((f))	S5	41500	11.1	37	2900	1.32	D3[a]	70	0.493	29.9	47
341	KGK2010 1	G080.8621+00.9749	O9V	S3	31500	7.7	18	1300	1.32	D3[a]	20	0.141	5.0	31
342	KGK2010 2	G080.9020+00.9828	B1V:	S3	26000	6	10	800	1.32	D3[a]	10	0.070	57.8	14
344	BD +43 3654	G082.4100+02.3254	O4If	S6	40700	19	58	3000	1.32	D3[a]	193	1.359	58.6	170
368	KM Cas	G134.3552+00.8182	O9.5V((f))	S7	30500	7.4	16	1200	1.95	D4[b]	14	0.146	24.9	22
369	BD +60 586	G137.4203+01.2792	O7.5V/O8III	S8	34400	8.9	24	2500	1.95	D4[b]	73	0.759	7.9	39
380	HD 53367	G223.7092−01.9008	B0IVe	S9	28000	7	15	1200	0.26	D1	15	0.021	35.7	49
381	HD 54662	G224.1685−00.7784	O7Vzvar?[c]	S1	35500	9.4	26	2500	0.63	D1	220	0.739	4.6	200
382	FN CMa	G224.7096−01.7938	B0III	S9	28000	15	20	1200	0.94	D1	101	0.506	11.2	70
406	HD 92607	G287.1148−01.0236	O9IVn	S1	31100	10	20	1300	2.35	D5[d]	16	0.201	29.1	26
407	HD 93249	G287.4071−00.3593	O9III+O:	S1	30700	13.6	23	1300	2.35	D5[d]	7.8	0.098	58.2	25
409	HD 93027	G287.6131−01.1302	O9.5IVvar[e]	S10	30300	10	16	1200	2.35	D5[d]	7.4	0.093	20.8	17
410	HD 305536	G287.6736−01.0093	O9.5V+?[f]	S1	30500	7.4	15	1200	2.35	D5[d]	3.7	0.046	91.4	14
411	HD 305599	G288.1505−00.5059	O9.5V	S11	30500	7.4	15	1200	2.35	D5[d]	4.2	0.052	41.5	16
413	HD 93683	G288.3138−01.3085	O9V+B0V[g]	S11	31500	7.7	18	1300	2.35	D5[d]	15	0.188	15.4	24

Notes. (1) Identifier from Kobulnicky et al. (2016), (2) common name, (3) generic identifier in galactic coordinates, (4) spectral classification, (5) reference for spectral classification, (6) effective temperature based on spectral classification using the theoretical scale of Martins et al. (2005a), (7) stellar radius based on spectral classification using the theoretical scale of Martins et al. (2005a), (8) adopted stellar mass, (9) adopted terminal wind velocity from Mokiem et al. (2007), (10) adopted distance, (11) reference for distance, (12) standoff distance in arcsec, (13) standoff distance in pc using the adopted distance and angular size from Kobulnicky et al. (2017) adjusted by a statistical factor of 1.1 for projection effects, (14) peak 70 μm surface brightness above adjacent background, (15) angular diameter of the nebula in arcsec defined by a chord intersecting the location of peak surface brightness. References for spectral types: S1—Sota et al. (2014); S2—Evans et al. (2005); S3—Chick et al. (2017); S4—Vijapurkar & Drilling (1993); S5—Hanson (2003); S6—Comerón & Pasquali (2007); S7—Massey et al. (1995); S8—Hillwig et al. (2006) gives O7.5V but Conti & Leep (1974) lists O8III; S9—Tjin A Djie et al. (2001); S10—Sota et al. (2011); S11—Alexander et al. (2016) References for Distances; D1—van Leeuwen (2007); D2—Hillenbrand et al. (1993); D3—Kiminki et al. (2015); D4—Xu et al. (2006); D5—Smith (2006).

[a] Assumed to be at a similar distance as Cygnus OB2 (Kiminki et al. 2015) based on similar magnitude and reddening, but see notes in text on KGK2010 10.

[b] Assumed to be in the Perseus spiral arm as part of the Cas OB6 Association near the W3/W4/W5 star-forming regions having maser parallax measurements by Xu et al. (2006). This is consistent with the open cluster photometric distance of 2.2 ± 0.2 kpc (Lim et al. 2014).

[c] The possible double-lined nature (O6.5V+O7-9V 2119 d period) of this source was reported by Boyajian et al. (2007) but was not confirmed by Sota et al. (2014).

[d] Understood to be part of the Carina Nebula complex at 2.35 kpc distance (Smith 2006), consistent with other contemporary determinations.

[e] A single-lined eclipsing binary according to Sota et al. (2011), suggesting a significant difference in mass between the primary and secondary star.

[f] A possible single-lined spectroscopic binary according to Levato et al. (1990).

[g] A double-lined spectroscopic binary according to Alexander et al. (2016).

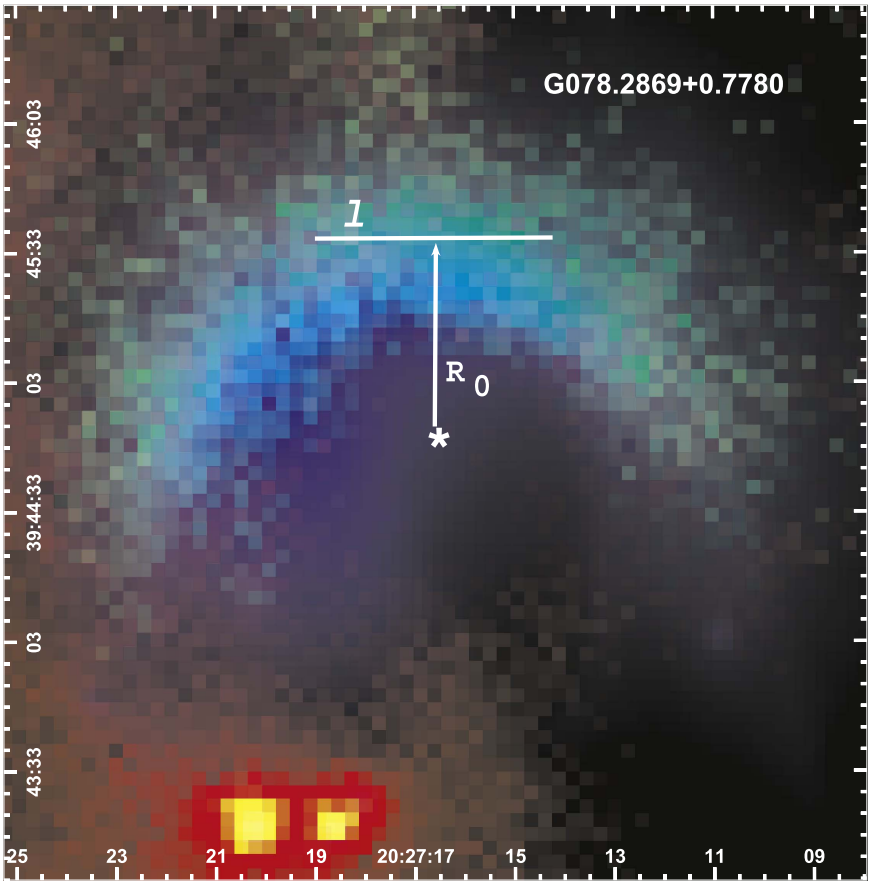

Figure 1. Three-color representation of the G078.2869+00.7780 nebula (object #331 from the catalog of Kobulnicky et al. 2016) with blue/green/red representing 24/70/160 μm from *SST*/*HSO*/*HSO*, respectively. White lines represent the standoff distance, R_0, and the chord diameter, ℓ.

from knowledge of the infrared surface brightness (i.e., specific intensity), the dust emissivity, the line-of-sight path length through the nebula, and a reasonable assumption for the gas-to-dust ratio. Here, I_ν is the specific intensity at a selected infrared frequency in erg s^{-1} cm^{-2} sr^{-1}, such as the *HSO* 70 μm band, where the optical depth of dust is thought to be low for essentially all Galactic sight lines; I_ν is directly measurable from the *HSO* images in Jy sr^{-1}. The path length through the dust nebula is ℓ, calculated from the projected angular diameter of the chord in radians, ℓ_r, times the adopted distance, D. This assumes rotational symmetry of the nebula such that the line-of-sight depth is adequately represented by the projected diameter. The dust emission coefficient per nucleon, j_ν, in Jy cm^2 sr^{-1} nucleon^{-1} as tabulated by Draine & Li (2007),[7] is determined by fitting their dust models to the infrared spectral energy distribution for each object, as performed in Kobulnicky et al. (2017) for the tabulated list of 20 objects. The Draine & Li (2007) Milky Way dust models assume a standard 1:136 dust grain to atomic particle (principally H + He) ratio, so the models provide directly the desired nucleon number density within the infrared nebulae:

$$n_N = \frac{I_\nu}{\ell\, j_\nu}. \tag{4}$$

[7] Note that Draine & Li (2007) use the emission coefficient, j_ν, to express the energy emitted per second per steradian per hertz per *nucleon* instead of the conventional definition of energy emitted per second per steradian per hertz *per volume*.

This is really an *average* density along the chord length intersecting the bow shock apex; the peak density near the apex of the bow shock could be larger. However, we desire to measure the *ambient* ISM density preceding the bow shock, n_a, not n_N. A physically motivated conversion would be $n_a = 0.25 n_N$, given that the density increases by a factor of four across a strong shock (e.g., Landau & Lifshitz 1987), which we expect given the highly supersonic nature of the >1000 km s^{-1} stellar winds. Therefore,

$$n_a = \frac{0.25 I_\nu}{\ell\, j_\nu}. \tag{5}$$

With these substitutions, Equation (3) then becomes

$$\dot{M} = \frac{4\pi R_{0r}^2 D^2 V_a^2 I_\nu 0.25 \bar{m}}{V_w \ell_r D j_\nu}, \tag{6}$$

which eliminates one factor of distance, D, and simplifies to

$$\dot{M} = \frac{\pi \bar{m} R_{0r}^2 D V_a^2 I_\nu}{V_w \ell_r j_\nu}. \tag{7}$$

In convenient astrophysical units, this can be expressed as a mass-loss rate in solar masses per year:

$$\dot{M}(M_\odot\ \mathrm{yr}^{-1}) = 1.67 \times 10^{-28} \times \frac{[R_0(\mathrm{arcsec})]^2\, D(\mathrm{kpc})\, [V_a(\mathrm{km\ s}^{-1})]^2\, I_\nu(\mathrm{Jy\ sr}^{-1})}{V_w(\mathrm{km\ s}^{-1})\, \ell(\mathrm{arcsec})\, j_\nu(\mathrm{Jy\ cm}^2\ \mathrm{sr}^{-1}\mathrm{nucleon}^{-1})}. \tag{8}$$

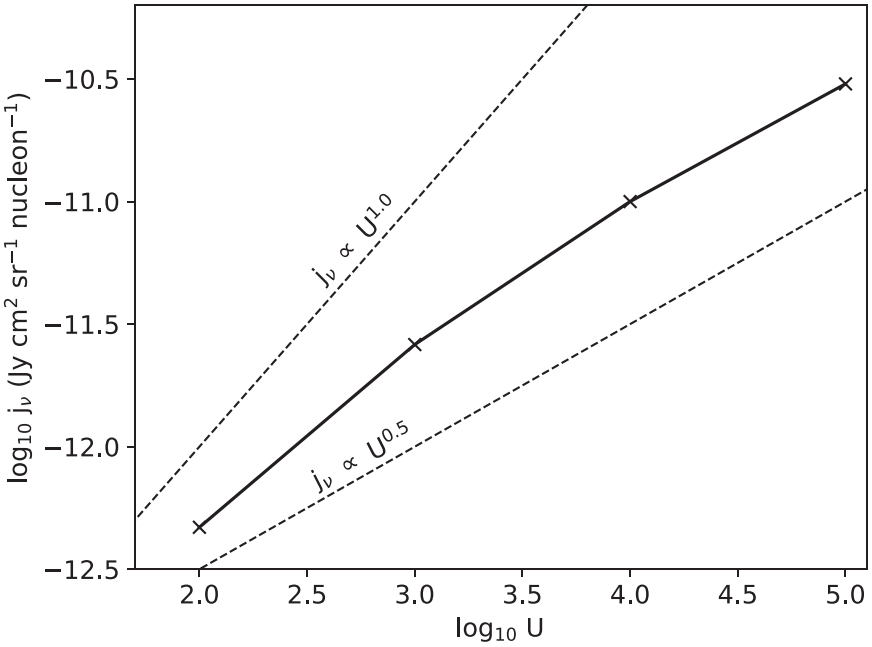

Figure 2. Base-10 logarithm of the DL07 model emission coefficient, j_ν, vs. radiation density parameter, U (solid line and crosses). The dashed lines show, for reference, power-law descriptions $j_\nu \propto U^{1.0}$ and $j_\nu \propto U^{1.0}$.

This expression is linear in all of the crucial quantities except the relative velocity between star and ISM and the angular standoff distance. The angular quantities R_{0r} and ℓ_r are measured to about 10% from infrared images. Here, I_ν is measured to about 20%, the dominant source of uncertainty being the definition of a suitable local background level. Mean stellar wind velocities are also measured to, perhaps, 50%. For this subsample, distances are known to better than 25% in the majority of cases. The stellar space velocities are approximations based on mean values for runaway stars; these may not be known to better than a factor of two. This makes the error budget on $\dot{M}$ nearly 60%, neglecting stellar velocity uncertainty, or about factor of two with it included. The model-dependent choice of j_ν is the most significant remaining variable.

Draine & Li (2007) provide a grid of models for interstellar dust, yielding j_ν as a function of wavelength and as a function of incident radiant energy density, U. The models are parameterized in terms of three variables: $U_{\rm min}$, the minimum radiant energy density[8] to which dust is exposed; a maximum radiant energy density $U_{\rm max}$ to which dust is exposed; and a fraction of polycyclic aromatic hydrocarbon (PAH) molecules by mass, $q_{\rm PAH}$, within the material. Kobulnicky et al. (2017) fitted DL07 models to the infrared spectral energy distributions of objects from Table 1, concluding that, in the majority of cases, models with a single radiant energy density (i.e., $U_{\rm min} = U_{\rm max}$) provided the best match to the data. They also tabulated an estimate for U in each nebula, calculated from the star's luminosity and standoff distance, assuming that the central star was the dominant source of illumination. Typical values for U ranged from a few $\times 10^2$ to a few $\times 10^4$, lending credence to the proposition that the central star dominates the energetics of each nebula. Furthermore, models with the minimum PAH mass fraction, $q_{\rm PAH} = 0.47\%$, were preferred, suggesting that PAHs are either destroyed or not present in the bow shock nebulae. Accordingly, we adopt for each object the emission coefficient, j_ν, given for the bandpass-averaged *HSO PACS*[9] 70 μm band from the single-U DL07 model appropriate to the U for each object. Because DL07 provides models only at discrete radiant energy densities of $U = 10^2$, 10^3, 10^4, 10^5, we employ linear interpolation to obtain a j_ν appropriate to each object.

Figure 2 plots the DL07 model emission coefficients versus the radiation density parameter (solid line and crosses). The dashed lines show, for reference, power-law descriptions $j_\nu \propto U^{1.0}$ and $j_\nu \propto U^{0.5}$. Figure 2 shows that, over the range of U covered by sample objects, j_ν is approximately proportional to $\sqrt{U}$. This means that j_ν is relatively insensitive to the adopted U. Note that U itself is proportional to $R_*^2\, T_{\rm eff}^4 / R_0^2$, where R_* is the stellar radius, $T_{\rm eff}$ is the effective stellar temperature, and R_0 is the standoff distance, which we previously expressed as $R_{0r}\, D$. This means that our estimate of j_ν implicitly contains a dependence on these quantities:

$$j_\nu \propto \sqrt{U} \propto \sqrt{\frac{R_*^2\, T_{\rm eff}^4}{R_{0r}^2 D^2}} = \frac{R_*\, T_{\rm eff}^2}{R_{0r} D}. \quad (9)$$

It can now be seen that Equation (7) goes as

$$\dot{M} \propto \frac{\bar{m} R_{0r}^3 D^2 V_a^2 I_\nu}{V_w \ell_r R_* T_{\rm eff}^2}, \quad (10)$$

so this expression of the mass-loss rate ultimately entails something close to a D^2 dependence, via the emission coefficient. Accordingly, our analysis here is restricted to objects that have well-constrained distances. If we characterize j_ν (via the DL07 models and knowledge of R_* and $T_{\rm eff}$) as

[8] U is defined in Draine & Li (2007) as the ratio of the incident radiant energy density (in erg cm^{-3}) to the mean interstellar radiant energy density estimated by Mathis et al. (1983).

[9] Photoconductor Array Camera and Spectrometer (PACS; Poglitsch et al. 2010).

Table 2
Derived Parameters for Stars and Their Bow Shock Nebulae

ID	Name	Alt. name	Sp.T.	Lum. (10^4 $L_\odot$)	U	j_ν (Jy sr^{-1} cm^2 nuc^{-1})	n_a (cm^{-3})	$\dot{M}$ ($M_\odot$ yr^{-1})
(1)	(2)	(3)	(4)	(5)	(6)	(7)	(8)	(9)
13	ζ Oph	G006.2812+23.5877	O9.2IV	8.1	4.2×10^3	8.7×10^{-12}	2.3	5.4×10^{-8}
67	NGC 6611 ESL 45	G017.0826+00.9744	O9V	5.1	1.3×10^4	1.1×10^{-11}	32	6.2×10^{-8}
329	KGK2010 10	G077.0505−00.6094	O8V+?	7.9	2.7×10^3	8.4×10^{-12}	1.3	2.5×10^{-8}
331	LS II +39 53	G078.2869+00.7780	O7V	12.0	2.2×10^3	8.3×10^{-12}	6.6	4.5×10^{-8}
338	CPR2002A10	G078.8223+00.0959	O8V:	7.9	4.9×10^3	8.9×10^{-12}	72	3.3×10^{-7}
339	CPR2002A37	G080.2400+00.1354	O5V((f))	32.0	2.1×10^3	8.3×10^{-12}	21	3.1×10^{-7}
341	KGK2010 1	G080.8621+00.9749	O9V	5.1	4.2×10^3	8.7×10^{-12}	15	1.4×10^{-8}
342	KGK2010 2	G080.9020+00.9828	B1V:	1.4	4.7×10^3	8.9×10^{-12}	160	1.4×10^{-7}
344	BD +43 3654	G082.4100+02.3254	O4If	87.0	7.6×10^2	8.0×10^{-12}	19	1.3×10^{-6}
368	KM Cas	G134.3552+00.8182	O9.5V((f))	4.1	3.2×10^3	8.5×10^{-12}	21	7.7×10^{-8}
369	BD +60 586	G137.4203+01.2792	O7.5V	9.7	2.7×10^2	7.8×10^{-12}	18	1.9×10^{-7}
380	HD 53367	G223.7092−01.9008	B0IVe	2.6	9.9×10^4	3.0×10^{-11}	16	2.2×10^{-9}
381	HD 54662	G224.1685−00.7784	O7Vzvar?	12.0	3.7×10^2	7.9×10^{-12}	1.2	6.4×10^{-8}
382	FN CMa	G224.7096−01.7938	B0III	12.0	7.7×10^2	8.0×10^{-12}	18	2.9×10^{-7}
406	HD 92607	G287.1148−01.0236	O9IVn	8.2	3.3×10^3	8.5×10^{-12}	16	1.1×10^{-7}
407	HD 93249	G287.4071−00.3593	O9III+O:	14.0	2.5×10^4	1.3×10^{-11}	12	3.5×10^{-8}
409	HD 93027	G287.6131−01.1302	O9.5IVvar	7.4	1.4×10^4	1.1×10^{-11}	9	2.2×10^{-8}
410	HD 305536	G287.6736−01.0093	O9.5V+?	4.1	3.1×10^4	1.5×10^{-11}	29	2.1×10^{-8}
411	HD 305599	G288.1505−00.5059	O9.5V	4.1	2.4×10^4	1.3×10^{-11}	6	1.2×10^{-8}
413	HD 93683	G288.3138−01.3085	O9V+B0V	5.1	2.4×10^3	8.3×10^{-12}	11	5.7×10^{-8}

Note. (1) Identifier from Kobulnicky et al. (2016), (2) common name, (3) generic identifier in galactic coordinates, (4) spectral classification, (5) stellar luminosity computed from effective temperature and radius in Table 1, (6) dimensionless ratio of the radiant energy density (in erg cm^{-3}) from the star to the mean interstellar radiant energy density estimated by Mathis et al. (1983, MMP83), as tabulated by Kobulnicky et al. (2017), (7) dust emission coefficient expressing the energy emitted per second per steradian per hertz per *nucleon*, (8) ambient interstellar number density, computed from Equation (5), (9) computed mass-loss rate in solar masses per year.

uncertain at the 30% level, the error budget for Equation (7) grows to about 70%, or a factor of two if stellar velocity uncertainties are included. Accordingly, we estimate the uncertainties on $\dot{M}$ to be 0.3 dex for this sample. Deviation of the mean stellar space velocities from the adopted $V_a = 30\,\mathrm{km\,s^{-1}}$ (not included in the above error budget) would represent a systematic error shifting the mass-loss rates by a factor V_{30}^2, where V_{30} is the relative star–ISM velocity in units of $30\,\mathrm{km\,s^{-1}}$.

3. Calculation of Mass-loss Rates and Comparison to Prior Estimates

Table 2 lists quantities derived from the basic data in Table 1. Columns 1–4 contain the identifying numeral, name, generic name, and spectral type, as in Table 1. Column 5 contains the stellar luminosity in units of 10^4 solar luminosities. Column 6 contains the radiation density parameter, U, calculated from the basic data. Column 7 lists the corresponding emission coefficient interpolated from the DL07 models. Column 8 is the ambient interstellar number density, n_a, derived from the 70 μm specific intensity, as described in the previous section. Densities range between 1.2 cm^{-3} and 160 cm^{-3}, with a median value of 16 cm^{-3}. These are typical of densities within the cool, neutral phase (≈30 cm^{-3}) of the ISM and somewhat higher than the warm, neutral phase (≈0.6 cm^{-3}) (see Draine 2011, Table 1.3). Column 9 contains the mass-loss rate calculated from Equation (7). Values range from 2×10^{-9} $M_\odot$ yr^{-1} to 1.3×10^{-6} $M_\odot$ yr^{-1}, with a median of 6×10^{-8} $M_\odot$ yr^{-1}. These are consistent with the broad range of mass-loss rates for O stars found in the literature and obtained using other methods.

It is particularly instructive to compare our results for the well-studied prototypical bow shock star ζ Oph with other analyses.[10] Our inferred density of 2.3 cm^{-3} compares favorably with the 3.6 cm^{-3} computed by Gvaramadze et al. (2012) and the ≃3 cm^{-3} estimated from the radio free–free and Hα surface brightness of the surrounding H II region (Gull & Sofia 1979). The resulting mass-loss rate is $\dot{M} = 5.4 \times 10^{-8}$ $M_\odot$ yr^{-1}. For comparison, Gull & Sofia (1979) report $\dot{M} = 2.2 \times 10^{-8}$ $M_\odot$ yr^{-1} using similar physical reasoning. Gvaramadze et al. (2012) list an identical $\dot{M} = 2.2 \times 10^{-8}$ $M_\odot$ yr^{-1}. Our value is almost a factor of 30 larger than the $\dot{M} = 1.8 \times 10^{-9}$ $M_\odot$ yr^{-1} inferred by Marcolino et al. (2009) by fitting model atmospheres to UV and optical wind lines. Our result is a factor of 2.4 smaller than the $\dot{M} = 1.3 \times 10^{-7}$ $M_\odot$ yr^{-1} predicted from the prescription of Vink et al. (2001) for the luminosity and temperature of ζ Oph. Predictions from the updated moving reversing layer theory (Lucy & Solomon 1970) by Lucy (2010b, Table 1) for the adopted parameters of ζ Oph ($T_{\rm eff} = 31{,}000$ K, $\log g = -3.75$) indicate $\dot{M} = 5.0 \times 10^{-8}$ $M_\odot$ yr^{-1}, in excellent agreement with our value. This agreement is all the more impressive given that ζ Oph is regarded as a weak-winded O star. Given the general consistency of the momentum-balance technique with theoretical expectations and some other mass-loss measurements for this prototypical bow shock star, we proceed to use the results from Table 2 to assess its general applicability to mass loss from massive stars.

[10] We note here that the angular standoff distance for ζ Oph is incorrectly listed in Table 5 of Kobulnicky et al. (2017) and Table 1 of Kobulnicky et al. (2016) as 29″ instead of 299″, making the linear distance 0.159 pc for the distance adopted here of 0.110 kpc.

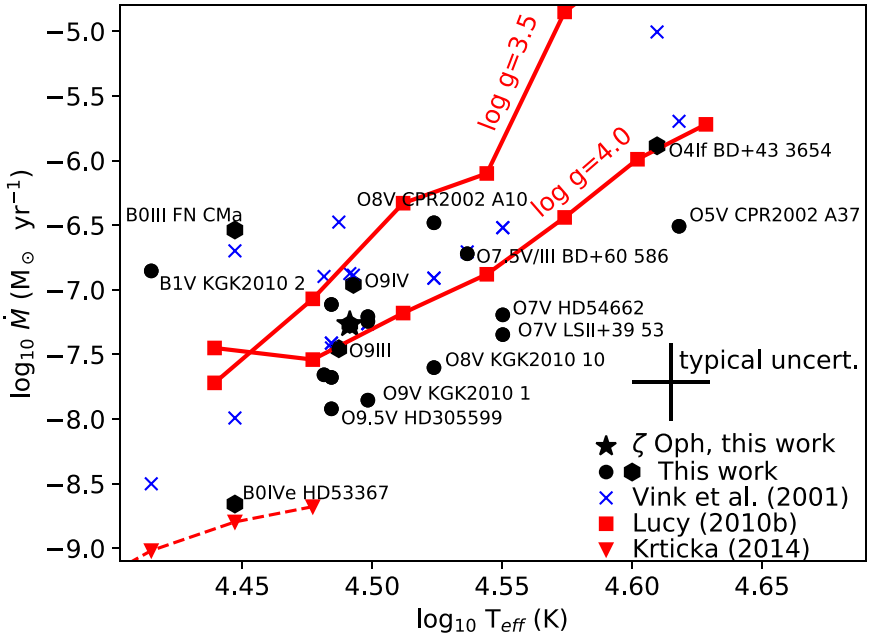

Figure 3. Mass-loss rate vs. stellar effective temperature. Black solid points and hexagons depict measurements for main-sequence and evolved stars from this sample, respectively. Blue crosses mark predictions for each object using the expression of Vink et al. (2001, Equation (24)). Red squares and lines show the model predictions of Lucy (2010b) for nominal main-sequence ($\log g = 4.0$) and giant ($\log g = 3.5$) stars, as labeled. The triangles and dotted lines show the theoretical predictions of Krtička (2014) for B stars.

Figure 3 plots the calculated mass-loss rates versus stellar effective temperature.[11] Black solid symbols denote the 20 sample objects: a star for ζ Oph, circles for main-sequence stars, and hexagons for evolved stars. Blue crosses depict model predictions for each object using the formulation of Vink et al. (2001, Equation (24)) computed using the stellar data from Table 1 and assuming $v_\infty/v_{\rm esc} = 2$. Hence, each solid data point is paired vertically with a blue x at the same temperature, although the s's sometimes overlap. Red squares connected by lines depict the model predictions from Lucy (2010b) for main-sequence ($\log g = 4.0$) and giant ($\log g = 3.5$) stars, as labeled. Red triangles and dotted lines show the predictions for B main-sequence stars from Krtička (2014). A cross above the legend depicts the typical measurement uncertainties on each axis. The dispersion in $\dot{M}$ at fixed temperature is 0.35 dex, roughly consistent with our stated uncertainties, but doubtless inflated by the inclusion of six objects in luminosity class IV/III among the sample of 20. Key objects are labeled with spectral type and common nomenclature.

Figure 3 demonstrates that there is good agreement between the Vink et al. (2001) and Lucy (2010b) predictions. Our new data fall ≈0.4 dex below the model predictions but follow the same trend of increasing mass-loss rate with effective temperature. The O4If star BD+43 3654 lies two orders of magnitude below the $\dot{M} > 10^5\ M_\odot\ {\rm yr}^{-1}$ levels predicted by the Lucy (2010b) relation for giants and an order of magnitude below the Vink et al. (2001) value for its temperature and luminosity. Objects O8V CPR2002 A10 and O7.5V/III BD +60 586 lie near the model predictions but at the upper envelope of the objects in our sample. In the former case, the spectral classification comes from our own yellow–red optical spectra (Chick et al. 2017), which are not especially sensitive to surface gravity. This object could be of a more evolved luminosity class, which would lead to an expected mass-loss rate more consistent with its position. The *Spitzer Space Telescope* 4.5/8.0/24 μm image of this object in Kobulnicky et al. (2016) reveals a nebula with very high surface brightness (indeed, the 70 μm surface brightness is the largest in our sample) that appears to be more like a partial bubble than a bow shock. The inferred ambient density of 72 cm^{-3} is an outlier and is the second largest in our sample. If this is a windblown bubble, meaning that the star's velocity is actually quite low (perhaps <10 km s^{-1} instead of the assumed 30 km s^{-1}), the resulting mass-loss rate would drop by a factor of 10 into the regime, consistent with other stars of the O8V classification. In the case of BD+60 586, Conti & Leep (1974) designate it as an O8III rather than O7.5V (Hillwig et al. 2006), which would explain its position at the high-$\dot{M}$ side of our sample.

Objects having O9–O9.5 spectral types form a tightly bunched vertical band in Figure 3 covering the range 10^{-8} $M_\odot$ yr^{-1} $< \dot{M} < 10^{-7}\ M_\odot$ yr^{-1}, a factor of two to three lower than both sets of models, on average. The three evolved stars (including ζ Oph) lie toward the upper end of this distribution. The dispersion in this subsample is somewhat larger than the 0.3 dex uncertainties, suggesting some degree of variation in mass-loss rates in this regime, although uncertainties on distance likely also play a role given that $\dot{M} \propto D^2$. We conclude that the data for late-O dwarfs (where the weak winds are observed to be common and the weak-wind problem is thought to be most pronounced), subdwarfs, and one giant show nearly an order of magnitude of dispersion and lie systematically below model predictions by a factor of about two, on average.

For the three early-B stars, the situation is less clear. The B0IVe star HD 53367 lies in the lower left of Figure 3 at $\dot{M} = 2.2 \times 10^{-9}\ M_\odot$ yr^{-1}, well below two of the three models, but in excellent agreement with the Krtička (2014) prediction.

[11] Although the mass-loss rate is expected to scale with *luminosity* rather than *temperature*, we choose here to plot the latter to facilitate direct comparison with the Lucy (2010a) models and because most of our targets are of similar V–IV luminosity class.

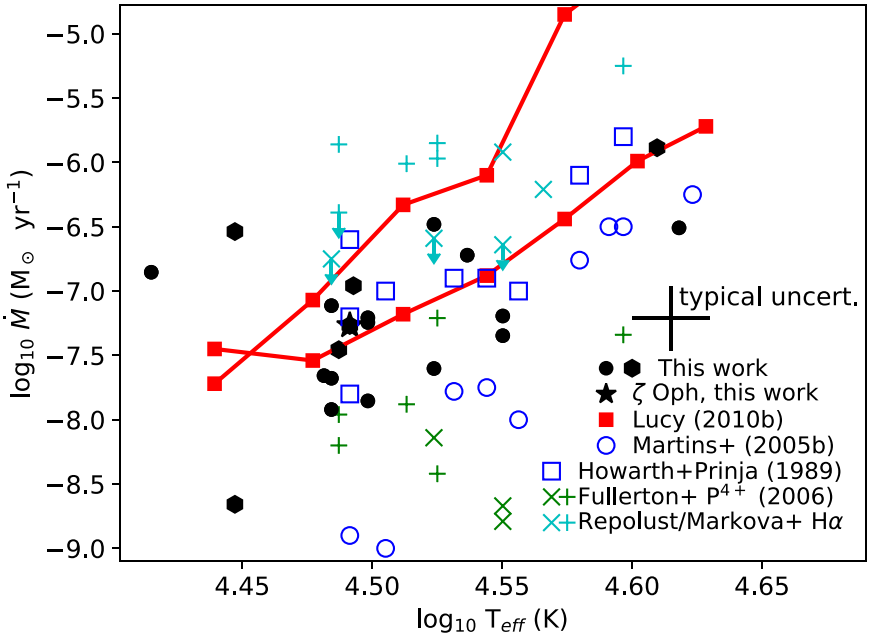

Figure 4. Mass-loss rate vs. stellar effective temperature, with symbols as in Figure 3. Open circles and squares depict the sample of galactic O3–O9 main-sequence stars as measured by Martins et al. (2005b) and Howarth & Prinja (1989), respectively. Green x's and +'s depict the dwarfs and giants, respectively, measured using the ultraviolet P^{4+} line (Fullerton et al. 2006). Cyan x's and +'s depict the same stars as determined from the Hα line.

The B0III star FN CMa lies nearly an order of magnitude above Lucy (2010b) model expectations and above the other data points but quite near the Vink et al. (2001) prediction at $\dot{M} = 2.9 \times 10^{-7}\ M_{\odot}\ \mathrm{yr}^{-1}$. Its prominent bow shock nebula appears well defined and well characterized. Its distance is somewhat poorly constrained by parallax at $0.94^{+1.1}_{-0.47}$ kpc. This may be a case where the space velocity is significantly different than the assumed 30 km s^{-1}. If its space velocity were to be much lower, perhaps 10 km s^{-1}, this object would be consistent with Lucy (2010b) model expectations and with the extrapolation of the trend defined by late-O stars. Finally, the B1V star KGK2010 2 lies an order of magnitude above the Vink et al. (2001) prediction, outside of the regime of the Lucy (2010b) models, and two orders of magnitude above the Krtička & Kubát (2017) prediction. This nebula has the third highest surface brightness in our sample and has one of the smallest standoff distances, making it very compact. Our multiple optical spectra of this star allow a range of spectral types, B2–B0, but the luminosity class is not well constrained. Its reddening and broadband magnitudes make it consistent with an early-B star at the 1.32 kpc distance of Cygnus OB2. A larger distance would only exacerbate the extremity of its apparent mass-loss rate. The infrared images of its nebula in Kobulnicky et al. (2016, 2017) show a strikingly bright and bow-shock-like morphology visible at 3.6 μm through 160 μm, making it one of the few objects among the 709-object bow shock catalog (Kobulnicky et al. 2016) detected across all seven *SST* and *HSO* infrared bandpasses. The inferred ambient number density of 160 cm^{-3} is, by far, the largest in our sample. This, coupled with the detection at even the shortest *SST* bandpasses, suggests an unusual interstellar environment. This object may be running into a molecular cloud, for instance. Kobulnicky et al. (2016) note that its infrared spectral energy distribution (SED) makes it one of the few objects better fit by a dust model with large PAH fraction, $q_{\mathrm{PAH}} = 4.58\%$. It has the coolest 24-to-70 μm color temperatures among the sample ($T_{24/70} = 70$ K; see Kobulnicky et al. 2017, Table 5). We attempted to use DL07 models having a larger PAH fraction with similar radiation density, but these yield smaller emission coefficients, which only serve to increase the resulting mass-loss rate. We conclude that the DL07 dust models may not be adequate in this case. Perhaps the PAHs and dust at the surface of a colder molecular structure are being fragmented in the wind shock, so the interstellar dust grain size distribution or grain composition adopted by DL07 is not appropriate here.

Figure 4 replicates Figure 3 with the addition of mass-loss rates measured for the set of galactic O3–O9.5 dwarf stars studied separately by Martins et al. (2005b; blue open circles) and Howarth & Prinja (1989; blue open squares), respectively. The discrepancy discussed in Martins et al. (2005b) is obvious here, with the open squares lying 0.5–1.5 dex above the open circles.[12] The Martins et al. (2005b) mass-loss rates derived from UV spectra appear consistent with the bow shock sample at the upper end of the temperature range, but lie well below the bow shock sample in the O8–O9 regime. The mass-loss rates given by Howarth & Prinja (1989) are consistently higher than the observational results presented here at the same spectral type (black solid symbols), but there is considerable scatter and some overlap. The Howarth & Prinja (1989) values are broadly consistent with the theoretical expectations for dwarfs. Figure 4 also shows the late-O dwarf and giant stars with mass-loss rates determined from ultraviolet P^{4+} absorption lines (Fullerton et al. 2006; green x's and +'s, respectively) and the same set of stars determined from the Hα line (Markova et al. 2004; Repolust et al. 2004; cyan x's and +'s). The P^{4+} measurements show a large dispersion at any given effective temperature, but generally lie an order of magnitude below the bow shock sample. The Hα results lie significantly above the bulk of the data and models, although most of the points for dwarfs are upper limits and thus are formally consistent with the other data without providing strong constraints. These upper limits

[12] We have shifted the effective temperatures assigned by Martins et al. (2005b) by −2000 K for consistency with the O9.5V objects in our sample.

underscore the difficulty in measuring mass-loss rates for late-O stars using the Hα line.

4. Discussion and Conclusions

Mass-loss rates derived from the principle of momentum balance and those predicted by two theoretical frameworks (Vink et al. 2001; Lucy 2010b) in Figure 3 display a similar trend with effective temperature but are offset by an average factor of about two lower. Knowledge of the star's velocity, stellar wind velocity, ambient density, and bow shock size yield mass-loss rates in good agreement with the Howarth & Prinja (1989) UV analysis, but substantially larger than more modern analyses of UV spectra in conjunction with atmosphere models such as CMFGEN (Hillier & Miller 1998). Our results are factors of several lower than Hα-based measurements, uncorrected for clumping, consistent with current consensus that a correction by factors of several for clumping is required. That the dispersion in the present results and the overall slope and zero point of the $\dot{M}$–$T_{\rm eff}$ relation are similar to other techniques and models suggests promise for the momentum-balance method, employed here for the first time using a sizable sample. Concomitantly, this could be seen as an indirect validation of the DL07 emission coefficients for dust within bow shock nebulae, an environment where it cannot be taken for granted that the prescriptions for typical interstellar dust size distributions, compositions, PAH absorption cross sections, grain heat capacities, dielectric functions, and so on will apply. It would not be unreasonable, a priori, to expect that within bow shock nebulae shocks act to fragment grains (as we speculate in the case of KGK2010 2) so that the DL07 models are inappropriate. This is evidently not the case for the majority of our sample. Viewed from another perspective, the general agreement in Figure 3 could be seen as a validation of the Vink et al. (2001) and Lucy (2010b) theoretical predictions using an observational technique that is unaffected by effects like clumping that plague density-squared diagnostics or the ionization structure uncertainties associated with absorption-line diagnostics. It remains unclear whether the 0.2–0.4 dex offset between the theoretical expectations and the bow shock sample can best be reconciled by identifying a systematic problem with the bow shock formalism outlined here or by further refinement in the theoretical treatment of stellar winds. Mass-loss rates derived here lie closer to model expectations than other observational results, ameliorating, but not fully resolving, the weak-wind problem. This qualified success of the momentum-balance approach may be used to refine traditional mass-loss diagnostics for application to stars that lack bow shock nebulae (the vast majority!).

The disparity between various $\dot{M}$ determinations evidenced in Figure 4 reflects the historical measurement problems discussed extensively in the literature regarding late-O stars. Resolving disparities with n^2 methods such as Hα is generally attempted by invoking ad hoc wind clumping factors of several (Fullerton et al. 2006; Prinja & Massa 2010). Resolving disparities with UV absorption diagnostics coupled with theoretical model atmospheres has been attempted by invoking modifications of the ionization structure (Lucy 2010b) or X-ray ionized winds (Huenemoerder et al. 2012). While the new measurements here do not help identify specific problems with classical $\dot{M}$ measurements, the self-consistency, lack of adjustable parameters, and better agreement with recent theoretical developments may help in revising those techniques.

The inferred interstellar ambient densities in Table 2 provide some insight regarding the conditions where bow shocks form. Peri et al. (2012, 2015) concluded that only 10%–15% of high-proper-motion massive stars showed evidence of infrared bow shocks. Huthoff & Kaper (2002) argued that interstellar density likely plays a larger role than space velocity or stellar spectral type in creating an observable nebula, a conclusion supported by the hydrodynamical simulations of Comeron & Kaper (1998) and Meyer et al. (2016). They found that slightly supersonic velocities, strong stellar winds, and larger ambient interstellar densities $n_a > 0.1$ cm^{-3} resulted in the visible bow shock nebulae. Our range of densities runs from $n_a = 1.2$ to 160 cm^{-3} with a mean of $n_a = 24$ cm^{-3}. ζ Oph has the second lowest density with $n_a = 2.3$ cm^{-3}. Its 70 μm surface brightness is the lowest in our sample, leading Kobulnicky et al. (2017) to note that it would not likely be detectable if it were not located 23° above the Galactic plane in a region of low infrared background. For most of the objects that lie within a degree of the plane, we infer that ambient densities of at least $n_a \gtrsim 5$ cm^{-3} appear to be required.

The uncertainties on our measurements are dominated, at present, by the lack of data on space velocities for each star in the frame of the local ISM. Because mass-loss rates scale as V_a^2, our adoption of a single $V_a = 30$ km s^{-1} likely leads to significant errors in some cases. True three-dimensional space velocities and accurate distances, such as will be provided by the GAIA mission (Gaia Collaboration et al. 2016a), should be available for many stars of interest in the near future so that more precise mass-loss rates will be possible. We are presently conducting a spectroscopic survey of bow shock stars that will provide needed data (spectral classifications, stellar temperatures, radii, radial velocities) for a much larger sample. An enhanced sample of early-B stars will result from this work, so mass-loss rates in this low-temperature, weak-wind regime should finally be possible to determine.

This work has been supported by the National Science Foundation through grants AST-1412845 and AST-1560461 (REU). We thank Nathan Smith and an anonymous reviewer for suggestions that improved this manuscript.

Facilities: SST, *WISE*, *Herschel*, HIPPARCOS.

ORCID iDs

Henry A. Kobulnicky https://orcid.org/0000-0002-4475-4176
Matthew S. Povich https://orcid.org/0000-0001-9062-3583

References

Abbott, D. C., Bieging, J. H., & Churchwell, E. 1981, ApJ, 250, 645
Acreman, D. M., Stevens, I. R., & Harries, T. J. 2016, MNRAS, 456, 136
Alexander, M. J., Hanes, R. J., Povich, M. S., & McSwain, M. V. 2016, AJ, 152, 190
Blaauw, A. 1961, BAN, 15, 265
Boyajian, T. S., Gies, D. R., Dunn, J. P., et al. 2007, ApJ, 664, 1121
Castor, J., McCray, R., & Weaver, R. 1975, ApJL, 200, L107
Chevalier, R. A., & Irwin, C. M. 2011, ApJL, 729, L6
Chick, W. T., Kobulnicky, H. A., Schurhammer, D., et al. 2017, ApJ, in press
Comeron, F., & Kaper, L. 1998, A&A, 338, 273
Comerón, F., & Pasquali, A. 2007, A&A, 467, L23
Conti, P. S., & Leep, E. M. 1974, ApJ, 193, 113
Dessart, L., & Owocki, S. P. 2005, A&A, 437, 657

Draine, B. T. 2011, in Physics of the Interstellar and Intergalactic Medium, ed. B. T. Draine (Princeton, NJ: Princeton Univ. Press), 6
Draine, B. T., & Li, A. 2007, ApJ, 657, 810
Ebbets, D. 1982, ApJS, 48, 399
Evans, C. J., Smartt, S. J., Lee, J.-K., et al. 2005, A&A, 437, 467
Fullerton, A. W., Gies, D. R., & Bolton, C. T. 1996, ApJS, 103, 475
Fullerton, A. W., Massa, D. L., & Prinja, R. K. 2006, ApJ, 637, 1025
Gaia Collaboration, Brown, A. G. A., Vallenari, A., et al. 2016, A&A, 595, A2
Gaia Collaboration, Prusti, T., de Bruijne, J. H. J., et al. 2016, A&A, 595, A1
Garmany, C. D., Olson, G. L., van Steenberg, M. E., & Conti, P. S. 1981, ApJ, 250, 660
Gies, D. R., & Bolton, C. T. 1986, ApJS, 61, 419
Glatzel, W., Kiriakidis, M., Chernigovskij, S., & Fricke, K. J. 1999, MNRAS, 303, 116
Gull, T. R., & Sofia, S. 1979, ApJ, 230, 782
Gvaramadze, V. V., & Bomans, D. J. 2008, A&A, 490, 1071
Gvaramadze, V. V., Langer, N., & Mackey, J. 2012, MNRAS, 427, L50
Hanson, M. M. 2003, ApJ, 597, 957
Hillenbrand, L. A., Massey, P., Strom, S. E., & Merrill, K. M. 1993, AJ, 106, 1906
Hillier, D. J., & Miller, D. L. 1998, ApJ, 496, 407
Hillwig, T. C., Gies, D. R., Bagnuolo, W. G., Jr., et al. 2006, ApJ, 639, 1069
Howarth, I. D., & Prinja, R. K. 1989, ApJS, 69, 527
Huenemoerder, D. P., Oskinova, L. M., Ignace, R., et al. 2012, ApJL, 756, L34
Huthoff, F., & Kaper, L. 2002, A&A, 383, 999
Kiminki, D. C., Kobulnicky, H. A., Vargas Álvarez, C. A., Alexander, M. J., & Lundquist, M. J. 2015, ApJ, 811, 85
Kobulnicky, H. A., Chick, W. T., Schurhammer, D. P., et al. 2016, ApJS, 227, 18
Kobulnicky, H. A., & Fryer, C. L. 2007, ApJ, 670, 747
Kobulnicky, H. A., Gilbert, I. J., & Kiminki, D. C. 2010, ApJ, 710, 549
Kobulnicky, H. A., Kiminki, D. C., Lundquist, M. J., et al. 2014, ApJS, 213, 34
Kobulnicky, H. A., Schurhammer, D. P., Baldwin, D. J., et al. 2017, AJ, 154, 201
Kraus, M., Haucke, M., Cidale, L. S., et al. 2015, A&A, 581, A75
Krtička, J. 2014, A&A, 564, A70
Krtička, J., & Kubát, J. 2017, A&A, 606, A31
Kudritzki, R.-P., & Puls, J. 2000, ARA&A, 38, 613
Lamers, H. J. G. L. M., & Leitherer, C. 1993, ApJ, 412, 771
Landau, L. D., & Lifshitz, E. M. 1987, Fluid Mechanics (New York: Pergamon Press)
Langer, N. 1998, A&A, 329, 551
Leitherer, C. 1988, ApJ, 326, 356
Lépine, S., & Moffat, A. F. J. 1999, ApJ, 514, 909
Levato, H., Malaroda, S., Garcia, B., Morrell, N., & Solivella, G. 1990, ApJS, 72, 323
Lim, B., Sung, H., Kim, J. S., Bessell, M. S., & Karimov, R. 2014, MNRAS, 438, 1451
Ling, Z., Zhang, S. N., & Tang, S. 2009, ApJ, 695, 1111
Lucy, L. B. 2010a, A&A, 512, A33
Lucy, L. B. 2010b, A&A, 524, A41
Lucy, L. B., & Solomon, P. M. 1970, ApJ, 159, 879
Marcolino, W. L. F., Bouret, J.-C., Martins, F., et al. 2009, A&A, 498, 837
Markova, N., Puls, J., Repolust, T., & Markov, H. 2004, A&A, 413, 693
Martins, F., Schaerer, D., & Hillier, D. J. 2005a, A&A, 436, 1049
Martins, F., Schaerer, D., Hillier, D. J., et al. 2005b, A&A, 441, 735
Massa, D., Fullerton, A. W., & Prinja, R. K. 2017, MNRAS, 470, 3765
Massey, P., Johnson, K. E., & Degioia-Eastwood, K. 1995, ApJ, 454, 151
Massey, P., & Thompson, A. B. 1991, AJ, 101, 1408
Mathis, J. S., Mezger, P. G., & Panagia, N. 1983, A&A, 128, 212
Meyer, D. M.-A., van Marle, A.-J., Kuiper, R., & Kley, W. 2016, MNRAS, 459, 1146
Meynet, G., Chomienne, V., Ekström, S., et al. 2015, A&A, 575, A60
Meynet, G., Maeder, A., Schaller, G., Schaerer, D., & Charbonnel, C. 1994, A&AS, 103, 97
Miller, A. A., Chornock, R., Perley, D. A., et al. 2009, ApJ, 690, 1303
Mokiem, M. R., de Koter, A., Vink, J. S., et al. 2007, A&A, 473, 603
Muijres, L. E., de Koter, A., Vink, J. S., et al. 2011, A&A, 526, A32
Muijres, L. E., Vink, J. S., de Koter, A., Müller, P. E., & Langer, N. 2012, A&A, 537, A37
Müller, P. E., & Vink, J. S. 2014, A&A, 564, A57
Noriega-Crespo, A., van Buren, D., & Dgani, R. 1997, AJ, 113, 780
Nugis, T., Crowther, P. A., & Willis, A. J. 1998, A&A, 333, 956
Owocki, S. P., Castor, J. I., & Rybicki, G. B. 1988, ApJ, 335, 914
Owocki, S. P., Cranmer, S. R., & Gayley, K. G. 1996, ApJL, 472, L115
Pauldrach, A., Puls, J., & Kudritzki, R. P. 1986, A&A, 164, 86
Pecaut, M. J., & Mamajek, E. E. 2013, ApJS, 208, 9
Peri, C. S., Benaglia, P., Brookes, D. P., Stevens, I. R., & Isequilla, N. L. 2012, A&A, 538, A108
Peri, C. S., Benaglia, P., & Isequilla, N. L. 2015, A&A, 578, A45
Perryman, M. A. C., Lindegren, L., Kovalevsky, J., et al. 1997, A&A, 323, 49
Poglitsch, A., Waelkens, C., Geis, N., et al. 2010, A&A, 518, L2
Povich, M. S., Benjamin, R. A., Whitney, B. A., et al. 2008, ApJ, 689, 242
Prinja, R. K., Massa, D., & Fullerton, A. W. 2002, A&A, 388, 587
Prinja, R. K., & Massa, D. L. 2010, A&A, 521, L55
Puls, J., Kudritzki, R.-P., Herrero, A., et al. 1996, A&A, 305, 171
Puls, J., Markova, N., Scuderi, S., et al. 2006, A&A, 454, 625
Puls, J., Urbaneja, M. A., Venero, R., et al. 2005, A&A, 435, 669
Puls, J., Vink, J. S., & Najarro, F. 2008, A&ARv, 16, 209
Renzo, M., Ott, C. D., Shore, S. N., & de Mink, S. E. 2017, A&A, 603, A118
Repolust, T., Puls, J., & Herrero, A. 2004, A&A, 415, 349
Sana, H., de Mink, S. E., de Koter, A., et al. 2012, Sci, 337, 444
Sexton, R. O., Povich, M. S., Smith, N., et al. 2015, MNRAS, 446, 1047
Smith, N. 2006, ApJ, 644, 1151
Smith, N. 2014, ARA&A, 52, 487
Smith, N., & McCray, R. 2007, ApJL, 671, L17
Smith, N., & Owocki, S. P. 2006, ApJL, 645, L45
Sota, A., Maíz Apellániz, J., Morrell, N. I., et al. 2014, ApJS, 211, 10
Sota, A., Maíz Apellániz, J., Walborn, N. R., et al. 2011, ApJS, 193, 24
Tjin A Djie, H. R. E., van den Ancker, M. E., Blondel, P. F. C., et al. 2001, MNRAS, 325, 1441
van Buren, D., & McCray, R. 1988, ApJL, 329, L93
van Leeuwen, F. 2007, A&A, 474, 653
Vijapurkar, J., & Drilling, J. S. 1993, ApJS, 89, 293
Vink, J. S., de Koter, A., & Lamers, H. J. G. L. M. 2001, A&A, 369, 574
Vink, J. S., & Gräfener, G. 2012, ApJL, 751, L34
Walborn, N. R., Danks, A. C., Vieira, G., & Landsman, W. B. 2002, ApJS, 140, 407
Waldron, W. L. 1984, ApJ, 282, 256
Xu, Y., Reid, M. J., Zheng, X. W., & Menten, K. M. 2006, Sci, 311, 54
Yadav, A. P., & Glatzel, W. 2017, MNRAS, 471, 3245